



Supporting Online Material for

Brownian Motion of an Ellipsoid

Y. Han, A. M. Alsayed, M. Nobili, J. Zhang, T. C. Lubensky,* A. G. Yodh

*To whom correspondence should be addressed. E-mail: tom@physics.upenn.edu

Published 27 October, *Science* **314**, 626 (2006)
DOI: 10.1126/science.1130146

This PDF file includes:

Materials and Methods
SOM Text
Figs. S1 to S5
References

Supporting Online Material

Materials and Methods

The experiments used various batches of micrometer-sized PMMA (poly-methyl methacrylate) or PS (polystyrene) ellipsoids in water confined between two glass walls. The methods described in Ref.(1) are used to make both PS and PMMA ellipsoids. For example, we put 0.5% PS spheres into a 12% aqueous PVA (polyvinyl alcohol) solution in a Petri dish. After water is evaporated, we stretched the PVA film at about 130°C. PS or PMMA spheres embedded in the film can be stretched because their glass transition temperatures are below 130°C. After cooling to room temperature, we dissolved the PVA and obtained ellipsoids with $\sim 10\%$ polydispersity. Note that the initial PMMA or PS spheres must not be cross-linked in order for them to be stretched. We can further measure the size of ellipsoids by SEM or just optical microscope. The clean ellipsoids solution were stabilized by 7 mM SDS (sodium dodecyl sulfate) after the samples were sonicated and centrifuged. The ellipsoid surfaces are not uniformly charged because some non-charged inner parts of PS or PMMA come to the surface after stretching. The ellipsoids also should not have strong interaction with glass surfaces because the solution ionic strength is > 0.1 mM and the Debye screening length is < 30 nm. It is hard to estimate the ionic strength accurately in a thin cell because glass surfaces release Na^+ ions (2). Nevertheless, we found that adding 2 mM salt did not change the diffusion coefficients (see Figs. S3-S5).

The glass surfaces were rigorously cleaned in a 1:4 mixture of hydrogen peroxide and sulfuric acid by sonication. Typically 0.3 μL solution spread over the entire $1.8 \times 1.8 \text{ mm}^2$ coverslip area, and ellipsoids do not stick to the surfaces. The cell was sealed with UV cured adhesive (Norland 63).

When the cell thickness, H , is below a few micrometers, interference colors from two inner surfaces under white light illumination can be observed by eye or in the reflection mode of a microscope. When $H = 0$, the light path difference is $\Delta l = \lambda/2$ due to the half wavelength phase shift at the lower surface. Thus any wavelength component in the white light will yield a dark black color at $H = 0$. When $H > 0$, the reflection light in the normal direction is a mixture of light with various wavelengths, and the different wavelength contributes to the signal with different weights. Thus the white light interference from a wedge will be bands of colors which are the same as the Michel-Levy Chart (3). By comparing the measured color with the Michel-Levy Chart, we can read out the corresponding Δl and obtain $H = \Delta l / (2n_w)$ where n_w is the refractive index of water. In the Michel-Levy Chart, the color starts from black at $\Delta l = 0$ and changes from red to blue periodically along the Δl axis with period of 625 nm. To avoid misreading the color by one or more bands, we made a reference wedge or put dilute spacer spheres with known diameter between glass slides to establish a reference thickness. Because the illumination light of the microscope is not an ideal white light source, color bands may shift slightly. The error of Δl however, should be less than 625/2 nm, so that the error of H is less than

100 nm. Usually our sample thickness has less than 20 nm variation in the central 1 mm^2 area and has 1-2 μm variation over the whole $18 \times 18 \text{ mm}^2$ area. Thus, we can study the diffusion of ellipsoids at different H in one cell, see Figs. S3-S5. As is the case for Newton rings, the interference colors on the two tips and the center of the ellipsoid are different. From the color fluctuations on the ellipsoid, we found that the 2D confinement was quite strong and that ellipsoid tumbling in the vertical plane was weak.

Particle motion was recorded by a Hitachi KP-M1U CCD camera on a Leica-DMRX microscope to videotape at 30 frames/sec. In the dilute suspension, only one ellipsoid was visible in the $640 \times 480 \text{ pixel}^2 = 38.4 \times 51.2 \mu\text{m}^2$ field of view under $100\times$ objective during a 0.5 hour experiment. The built-in 2D Gaussian fit function in IDL (Interactive Data Language) was used to locate the center and orientation of the ellipse in each video frame. The spatial and angular resolutions are obtained from intercepts of MSDs (4).

SOM Text

Simulation

As shown in Eq.(4), the statistics of angular displacements and of spatial displacements in the body frame are Gaussian. We used these facts to perform simple simulations of random walks: Angular displacements and translational displacements along long and short axes were simulated by three computer-generated independent arrays of Gaussian random numbers. The variance of

each random number array is set as $2Dt$ where D is the appropriate diffusion coefficient D_a , D_b , or D_θ , and t is the time step, e.g. 1/30 s. We projected the resulting motion into the lab frame as shown in Fig. 1A and B with $D_a/D_b = 99$. Non-Gaussian parameters and the PDF for $D_a/D_b = 4.07$ were further calculated from the random steps as shown in Fig. 3.

Comparing with theoretical 3D results and the walls' effects

In Figs. S3-S5, we compared the measured diffusion coefficients in quasi-2D with theoretical predictions (5-7) in unconfined 3D. Specifically we plotted out their ratios of $D^{3D}/D = \gamma/\gamma^{3D}$ vs. the degree of confinement, and compared them with the available theoretical (7) or numerical (8) results (solid curves). As expected, we can see: 1) All ratios > 1 and positive slopes show that the diffusion is slower at stronger confinement; 2) The larger slopes of more needle-like ellipsoids indicate that their motions are more sensitive to the confinement; 3) Larger slopes in Fig. S4 compared to those in Fig. S3 indicate that the diffusion along the short axis is more strongly affected by the confinement.

Derivations of equations

Here we provide some details about the derivations of Eqs. (2), (3), (6), (8) and (10) in the text. These equations follow from the integration of Eq. (1) without external forces ($\partial\mathcal{H}/\partial x = 0$, $\partial\mathcal{H}/\partial\theta = 0$):

$$\partial_t x_i(t) = \xi_i(t) \tag{S1a}$$

$$\partial_t \theta(t) = \xi_\theta(t), \quad (\text{S1b})$$

where $\xi_\theta(t)$ is a Gaussian random variable with variance

$$\langle \xi_\theta(t) \xi_\theta(t') \rangle = 2k_B T \Gamma_\theta \delta(t - t') \equiv 2D_\theta \delta(t - t') \quad (\text{S2})$$

and $\xi_i(t)$ is a Gaussian random variable at fixed $\theta(t)$ (or equivalently fixed $\xi_\theta(t)$) with variance, which depends on the instantaneous angle $\theta(t)$,

$$\langle \xi_i(t) \xi_j(t') \rangle = 2k_B T \Gamma_{ij}(\theta(t)) \delta(t - t'), \quad (\text{S3})$$

where

$$\Gamma_{ij}(\theta) = \bar{\Gamma} \delta_{ij} + \frac{1}{2} \Delta \Gamma M_{ij}(\theta(t)) \quad (\text{S4})$$

and

$$M_{ij}(\theta) = \begin{pmatrix} \cos 2\theta & \sin 2\theta \\ \sin 2\theta & -\cos 2\theta \end{pmatrix}. \quad (\text{S5})$$

We first consider the properties of $\theta(t)$. From Eq. (S1b),

$$\theta(t) = \theta_0 + \int_0^t \xi_\theta(t') dt' \equiv \theta_0 + \Delta\theta(t). \quad (\text{S6})$$

Thus

$$\langle \Delta\theta(t) \Delta\theta(t') \rangle = 2D_\theta \int_0^t dt_1 \int_0^{t'} dt_2 \delta(t_1 - t_2) = 2D_\theta \min(t, t'), \quad (\text{S7})$$

where $\min(t, t')$ is the lesser of t and t' , and

$$\langle [\Delta\theta(t) - \Delta\theta(t')]^2 \rangle = 2D_\theta |t - t'|. \quad (\text{S8})$$

Because $\Delta\theta(t)$ is a Gaussian random variable, we can easily evaluate averages of exponentials:

$$\left\langle e^{i[n\Delta\theta(t) \pm m\Delta\theta(t')]} \right\rangle = e^{-D_\theta [n^2 t + m^2 t' \pm 2nm \min(t, t')]} \quad (\text{S9})$$

From this general formula, we can calculate

$$\langle \cos n\theta(t) \rangle = \text{Re} \langle e^{in[\theta_0 + \Delta\theta(t)]} \rangle = \cos n\theta_0 e^{-n^2 D_\theta t} \quad (\text{S10a})$$

$$\langle \sin n\theta(t) \rangle = \text{Im} \langle e^{in[\theta_0 + \Delta\theta(t)]} \rangle = \sin n\theta_0 e^{-n^2 D_\theta t}. \quad (\text{S10b})$$

With the preceding formulae for correlations of $\theta(t)$, we can calculate correlations in $x_i(t)$. We begin with the second moments:

$$\begin{aligned} \langle \Delta x_i(t) \Delta x_j(t) \rangle_{\theta_0} &\equiv \langle \Delta x_i(t) \Delta x_j(t) \rangle_{\theta_0}^{\xi_i, \xi_\theta} \\ &= \int_0^t dt_1 \int_0^t dt_2 \langle \xi_i(t_1) \xi_j(t_2) \rangle_{\theta_0}^{\xi_i, \xi_\theta} = \int_0^t dt_1 2k_B T \langle \Gamma_{ij}(\theta(t_1)) \rangle_{\theta_0}^{\xi_\theta}, \end{aligned} \quad (\text{S11})$$

where we have introduced superscripts ξ_i and ξ_θ to emphasize which of the noises are to be averaged and the subscript θ_0 to indicate that the averages are to be taken at fixed initial value of $\theta = \theta_0$. Thus, using Eq. (S10), we obtain Eq. (2) in the text:

$$\langle \Delta x_i(t) \Delta x_j(t) \rangle_{\theta_0} = 2\overline{D}t + \Delta D M_{ij}(\theta_0) \int_0^t dt' e^{-4D_\theta t'} = 2\overline{D}t + \Delta D M_{ij}(\theta_0) \tau_4(t), \quad (\text{S12})$$

where

$$\tau_n(t) = \int_0^t dt' e^{-nD_\theta t'} = \frac{1}{nD_\theta} (1 - e^{-nD_\theta t}). \quad (\text{S13})$$

The cross-correlation functions of Eq. (3) in the text are calculated as follows:

$$\begin{aligned} \langle \Delta x_i(t) \Delta x_j(t) e^{in\theta(t)} \rangle &= \int_0^t dt_1 \int_0^t dt_2 \langle \xi_i(t_1) \xi_j(t_2) e^{in\theta(t)} \rangle_{\theta_0} \\ &= 2k_B T \int_0^t dt_1 \left\langle \left[\overline{\Gamma} + \frac{\Delta \Gamma}{2} M_{ij}(\theta(t_1)) \right] e^{in\theta(t)} \right\rangle_{\theta_0}. \end{aligned} \quad (\text{S14})$$

Using Eq. (S9) and the fact that $t_1 < t$ so that $\min(t, t_1) = t_1$, we find

$$\langle e^{i[\pm 2\theta(t_1) + n\theta(t)]} \rangle_{\theta_0} = e^{i(n\pm 2)\theta_0} e^{-D_\theta[n^2 t \pm 4(n\pm 1)t_1]}, \quad (\text{S15})$$

thus

$$\langle \Delta x_i \Delta x_j e^{in\theta} \rangle / t = \left[2\bar{D} + \frac{\Delta D}{2} A_{ij}^{(n)}(t) \right] e^{in\theta_0 - n^2 D_\theta t} \quad (\text{S16})$$

where $A_{ij}^{(n)}(t) = e^{i2\theta} \tau_{(4+4n)} \begin{pmatrix} 1 & -i \\ -i & -1 \end{pmatrix} + e^{-i2\theta} \tau_{(4-4n)} \begin{pmatrix} 1 & i \\ i & -1 \end{pmatrix}$.

Next we calculate the fourth cumulant, $C_{\theta_0}^{(4)}(t)$, of $\Delta x(t)$ (Eq. (6) of the text). We first have to calculate the fourth moment of $\Delta x(t)$:

$$\begin{aligned} \langle [\Delta x(t)]^4 \rangle_{\theta_0} &= \int_0^t dt_1 \dots dt_4 \langle \xi_x(t_1) \xi_x(t_2) \xi_x(t_3) \xi_x(t_4) \rangle_{\theta_0} \\ &= 12(k_B T)^2 \int_0^t dt_1 \int_0^t dt_2 \langle \Gamma_{xx}(\theta(t_1)) \Gamma_{xx}(\theta(t_2)) \rangle_{\theta_0}^{\xi_\theta} \\ &= 12(k_B T)^2 \int_0^t dt_1 \int_0^t dt_2 \left(\bar{\Gamma}^2 + \frac{1}{2} \Delta \Gamma \bar{\Gamma} \langle \cos 2\theta(t_1) + \cos 2\theta(t_2) \rangle \right. \\ &\quad \left. + \frac{1}{4} (\Delta \Gamma)^2 \langle \cos 2\theta(t_1) \cos 2\theta(t_2) \rangle \right) \\ &= 12 \left(\bar{D}^2 t^2 + \Delta D \bar{D} \cos 2\theta_0 \tau_4(t) t \right. \\ &\quad \left. + (k_B T)^2 \frac{\Delta \Gamma^2}{4} \int_0^t dt_1 \int_0^t dt_2 \langle \cos 2\theta(t_1) \cos 2\theta(t_2) \rangle \right). \end{aligned} \quad (\text{S17})$$

Then, using $\cos 2\theta_1 \cos 2\theta_2 = [\cos 2(\theta_1 - \theta_2) + \cos 2(\theta_1 + \theta_2)]/2$ and

$$\langle \cos 2[\theta(t_1) - \theta(t_2)] \rangle = e^{-4D_\theta |t_1 - t_2|} \quad (\text{S18})$$

$$\langle \cos 2[\theta(t_1) + \theta(t_2)] \rangle = \cos 4\theta_0 e^{-4D_\theta(t_1 + t_2 + 2\min(t_1, t_2))}, \quad (\text{S19})$$

we obtain

$$\begin{aligned} \langle [\Delta x(t)]^4 \rangle_{\theta_0} &= 12 \left[\bar{D}^2 t^2 + \Delta D \bar{D} \cos 2\theta_0 \tau_4(t) t \right. \\ &\quad \left. + \frac{(\Delta D)^2}{8} \left(\tau_\theta(t - \tau_4(t)) + \cos 4\theta_0 \frac{\tau_\theta(\tau_4(t) - \tau_{16}(t))}{3} \right) \right] \end{aligned} \quad (\text{S20})$$

where $\tau_\theta = 1/(2D_\theta)$. Then using Eq. (S12) for $\langle[\Delta x(t)]^2\rangle$, we obtain Eq. (6) of the text:

$$\begin{aligned} C_{\theta_0}^{(4)}(t) &= \langle[\Delta x(t)]^4\rangle_{\theta_0} - 3\langle[\Delta x(t)]^2\rangle_{\theta_0}^2 \\ &= \frac{1}{2}(\Delta D)^2[3(\tau_\theta t - \tau_\theta \tau_4(t) - \tau_4(t)^2) \\ &\quad + (\tau_\theta \tau_4(t) - \tau_\theta \tau_{16}(t) - 3\tau_4(t)^2) \cos 4\theta_0]. \end{aligned} \quad (\text{S21})$$

The numerator of the non-Gaussian parameter $\bar{p}(t)$ in Eq. (8) is the 4th cumulant of $\Delta x(t)$ averaged over both the noises $\xi(t)$ and $\xi_\theta(t)$ and the initial angle θ_0 :

$$\begin{aligned} \bar{C}^{(4)}(t) &= \langle[\Delta x(t)]^4\rangle - 3\langle[\Delta x(t)]^2\rangle^2 \\ &= \frac{1}{2\pi} \int_0^{2\pi} \langle[\Delta x(t)]^4\rangle_{\theta_0} d\theta_0 - 3 \left[\frac{1}{2\pi} \int_0^{2\pi} \langle[\Delta x(t)]^2\rangle_{\theta_0} d\theta_0 \right]^2 \\ &= 12 \left[\bar{D}^2 t^2 + \frac{\Delta D^2}{8} (t - \tau_4) \tau_\theta \right] - 3 [2\bar{D}t]^2 = \frac{3}{2} \Delta D^2 (t - \tau_4) \tau_\theta. \end{aligned} \quad (\text{S22})$$

The generating function (characteristic function) of Δx at fixed θ_0

$$g_{\Delta x}(k, t, \theta_0) = \langle e^{-ik\Delta x(t)} \rangle_{\theta_0} = \exp \left[\sum_{n=0}^{\infty} \frac{1}{(2n)!} (-ik)^{2n} C_{\theta_0}^{(2n)}(t) \right] \quad (\text{S23})$$

provides further information about cumulants and non-Gaussian behavior. It is useful to carry out the average over $\xi_i(t)$ in the average of $g_{\Delta x}(k, t, \theta_0)$ before that over $\xi_\theta(t)$:

$$g_{\Delta x}(k, t, \theta_0) = \langle \langle e^{-ik\Delta x(t)} \rangle_{\xi_i} \rangle_{\theta_0}^{\xi_\theta} = \langle e^{-k^2 k_B T \int_0^t dt' \Gamma_{xx}(t', \theta(t))} \rangle_{\theta_0}^{\xi_\theta}. \quad (\text{S24})$$

We are particularly interested in small times, in which case, we can expand $\cos 2\theta(t)$ in powers of $\Delta\theta(t)$ to obtain

$$\Gamma_{xx}(t, \theta(t)) \approx \Gamma_{xx}(t, \theta_0) - \Delta\Gamma(\sin 2\theta_0 \Delta\theta(t) + \cos 2\theta_0 (\Delta\theta(t))^2), \quad (\text{S25})$$

where $\Gamma_{xx}(t, \theta_0) = \bar{\Gamma} + \frac{1}{2}\Delta\Gamma \cos 2\theta_0$. Thus, at small t ,

$$g_{\Delta x}(k, t, \theta_0) \approx e^{-k^2 D_{xx}(\theta_0)t} \langle e^{k^2 \Delta D [\sin 2\theta_0 \int_0^t dt' \Delta\theta(t') + \cos 2\theta_0 \int_0^t dt' [\Delta\theta(t')]^2 + \dots]} \rangle_{\theta_0}^{\xi_\theta}. \quad (\text{S26})$$

Because $\Delta\theta(t) \sim t^{1/2}$, the coefficient of k^{2n} in the cumulant expansion Eq. (S23) and the $(2n)^{\text{th}}$ cumulant vanishes at least as rapidly as $t^{3n/2}$ as $t \rightarrow 0$ for $n \geq 2$ or as t^{n+s_n} , where $s_n \geq n/2 > 0$. The first cumulant remains $D_{xx}(\theta_0)t$ to lowest order in t . This analysis of the generating function makes it clear that the origin of non-Gaussian behavior is the dependence of the dissipative coefficient $\Gamma_{ij}(t, \theta)$ on θ .

The derivation of Eq. (10) in the text requires some care. The distributions function can be expressed as

$$\begin{aligned} f_{\Delta x}(x) &= \langle \delta(x - \Delta x(t)) \rangle = \int_{-\infty}^{\infty} dk e^{ikx} \langle e^{-ik\Delta x(t)} \rangle \\ &= \int_{-\infty}^{\infty} dk e^{ikx} \int_0^{2\pi} \frac{d\theta_0}{2\pi} g_{\Delta x}(k, t, \theta_0) \\ &= \int_0^{2\pi} \frac{d\theta_0}{2\pi} \int_{-\infty}^{\infty} dk e^{ikx} e^{[(ik)^2 C_{\theta_0}^{(2)}(t)/2! + (ik)^4 C_{\theta_0}^{(4)}(t)/4! + \dots]}. \quad (\text{S27}) \end{aligned}$$

The full average $\langle \rangle$ is again an ensemble average at fixed θ_0 followed by a second average over all θ_0 . The second cumulant of Δx is $C_{\theta_0}^{(2)}(t) = \langle \Delta x^2(t) \rangle_{\theta_0} - \langle \Delta x(t) \rangle_{\theta_0}^2 = \langle \Delta x^2(t) \rangle_{\theta_0} - 0 = \sigma_{\Delta x^2}^2(\theta_0) \sim t$ at small t . In fact, at fixed θ_0 and small t , $\Delta x \approx \Delta a \cos \theta_0 - \Delta b \sin \theta_0$ where Δa and Δb are two sets of Gaussian random variables with respective variances $\sigma_a^2 = 2D_a t$ and $\sigma_b^2 = 2D_b t$. Thus $\sigma_{\Delta x}^2(\theta_0) = \sigma_a^2 \cos^2 \theta_0 + \sigma_b^2 \sin^2 \theta_0 \equiv \sigma^2(\theta_0)$. $(2n)^{\text{th}}$ order cumulants for $n > 2$ vanish for small t as t^{n+s_n} , where $s_n > 0$. After a change

of variables, $u = kt^{1/2}$, all the $(2n)^{\text{th}}$ cumulants with $n \geq 2$ vanish as $t \rightarrow 0$ because they are of order t^{n+s_n} , and

$$\begin{aligned} f_{\Delta x}(x) &\xrightarrow{t \rightarrow 0} \int_0^{2\pi} \frac{d\theta_0}{2\pi} \int_{-\infty}^{\infty} dk e^{ikx} e^{-k^2 \sigma^2(\theta_0)/2} \\ &= \int_0^{2\pi} \frac{d\theta}{2\pi} \frac{e^{-\frac{x^2}{2\sigma^2(\theta)}}}{\sqrt{2\pi\sigma^2(\theta)}}. \end{aligned} \quad (\text{S28})$$

The Fourier transform of the probability density function, *i.e.* the characteristic function of Δx , has a simple form:

$$\begin{aligned} g_{\Delta x}(k, t = 0) &= \langle e^{ik\Delta x} \rangle = \int_{-\infty}^{\infty} e^{ikx} f_{\Delta x}(x) dx \\ &= e^{-\frac{k^2}{2} \frac{\sigma_a^2 + \sigma_b^2}{2}} I_0 \left(\frac{k^2}{4} (\sigma_a^2 - \sigma_b^2) \right), \end{aligned} \quad (\text{S29})$$

where I_0 is the 0th order modified Bessel function of the first kind. Here the non-Gaussian behavior of Δx is clear: Eq. (S29) is not a Gaussian function of k except at $\sigma_a^2 = \sigma_b^2$ where $I_0(0) = 1$.

Supporting Figures

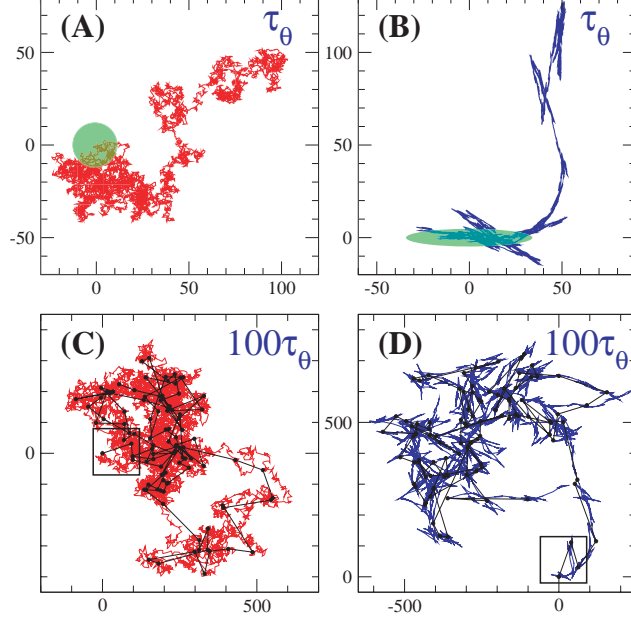


Figure S1: Simulations of 2D random walks for a sphere with diffusion coefficients $D_a = D_b = 0.5$ [(A) and (C)] and for an ellipsoid [(B) and (D)] with $D_a = 0.99, D_b = 0.01$. The total diffusion coefficient $D = (D_a + D_b) = 1.0$ is the same for both particles. (A) and (B): trajectories consisting of 10,000 steps with total duration τ_θ , the time it takes an ellipsoid to diffuse 1 radian. The initial positions of particles in (A) and (B) are represented, respectively, by a green circle and a green ellipsoid. (C) and (D): 10,000-step trajectories of total time duration $100\tau_\theta$. Also shown are coarse-grained 100-step trajectories in black. The trajectories of the sphere are self-similar random walks with fractal dimension 2 for all times. For times less than τ_θ , the dominant motion (B) of the ellipsoid is quasi-one-dimensional diffusion along its long axis. At times long compared to τ_θ , the coarse-grained trajectory of the ellipse is similar to that of the spherical particle: it corresponds to an isotropic random walk. The large value of $D_a/D_b = 99$ used in these simulations was chosen to emphasize the effects of anisotropy. The largest value of this ratio in our experiments is 4.07.

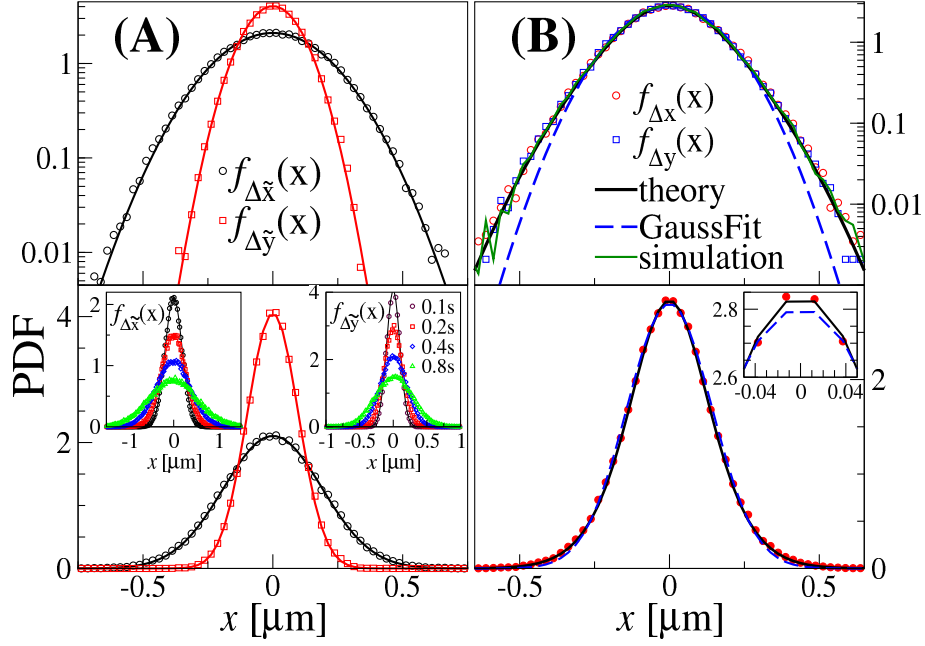


Figure S2: (A) Body-frame PDFs for $\Delta\tilde{x}(t)$ (circles) and $\Delta\tilde{y}(t)$ (squares) and (B) lab-frame PDFs for $\Delta x(t)$ and $\Delta y(t)$ at $t = 0.1$ s. The top figures are log-scale and the bottom linear-scale. Curves in (A) are Gaussian with widths $2D_a t$ and $2D_b t$. Insets show Gaussian behavior for 4 different times. In (B), the solid dark curve is the theoretical curve of Eq. (10) with no free parameter ($\sigma_a = \sqrt{2D_a t}$ with D_a from the fit of Fig. 2A). Dashed curve: the best Gaussian fit; Light curve [top only]: simulation; Solid circles [bottom only]: the average of $f_{\Delta x}(x)$ and $f_{\Delta y}(x)$ for better statistics. The inset to (D) is a blow-up of the region around $x = 0$.

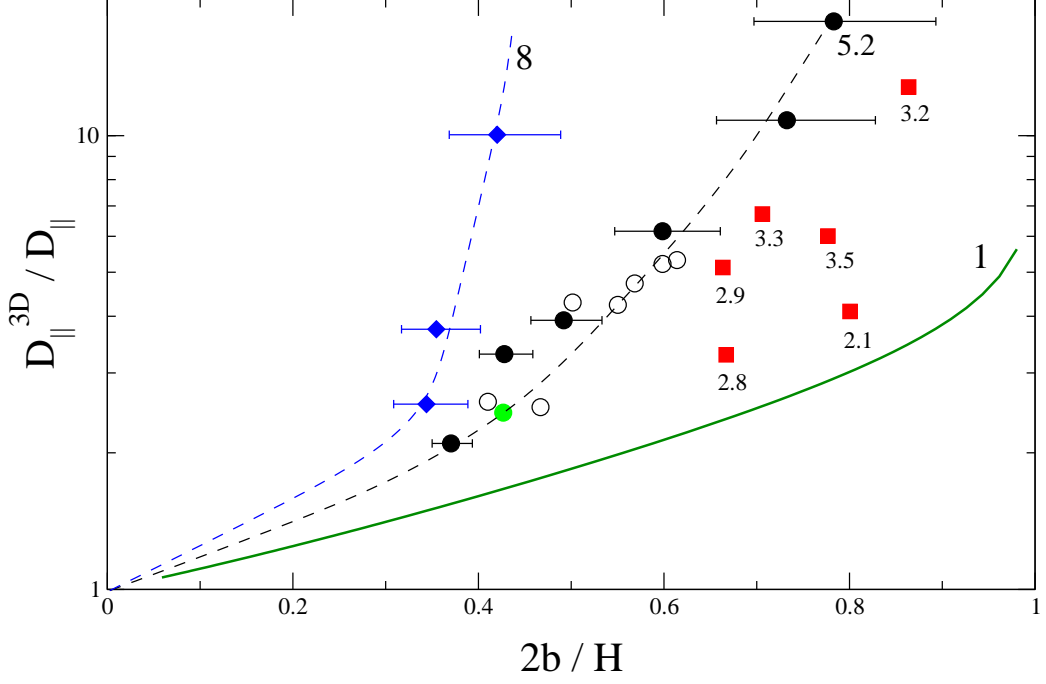


Figure S3: Ratio of theoretical diffusion coefficient (γ) along long axis D_{\parallel}^{3D} and measured diffusion coefficient D_{\parallel} under different confinement $2b/H$. $2b$ is the length of short axis of the ellipsoid and H is the separation of the two walls. Diamonds: $2.4 \times 0.3 \times 0.3 \mu\text{m}$ ellipsoids; Circles: $3.3 \times 0.635 \times 0.635 \mu\text{m}$ ellipsoids; Solid circles: no adding salt; Open circles: 2 mM adding salt; Green solid circle: BSA (bovine serum albumin) covered glass surface; Squares: polydispersed spheroids which aspect ratios are labeled below each data point, they have comparable error bars due to the 100 nm uncertainty in H . Although the absolute value of H may subject to 100 nm uncertainty, the relative values of different H are about 5 times more accurate. Dashed curve: guide to eyes; Solid curve: replot of Fig. 1 of Ref.(8) for numerical result of a sphere at $H/2$. We thank Jerzy Blawdziewicz for helpful discussions and for the data corresponding to the solid curve in the figure.

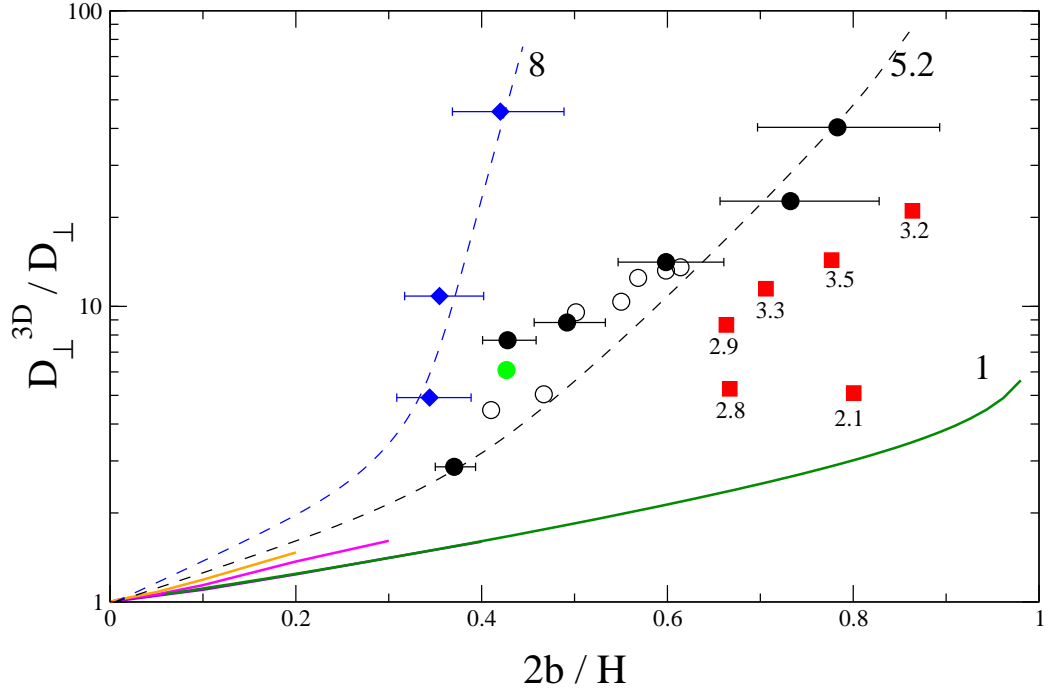


Figure S4: Ratio of theoretical diffusion coefficient (γ) along short axis D_{\perp}^{3D} and measured diffusion coefficient D_{\perp} under different confinement $2b/H$. Symbols are the same as those in Fig. S3. Solid curves from right to left: theoretical (γ) and numerical (δ) results for aspect ratio $a/b = 1, 2, 3$ under weak confinement.

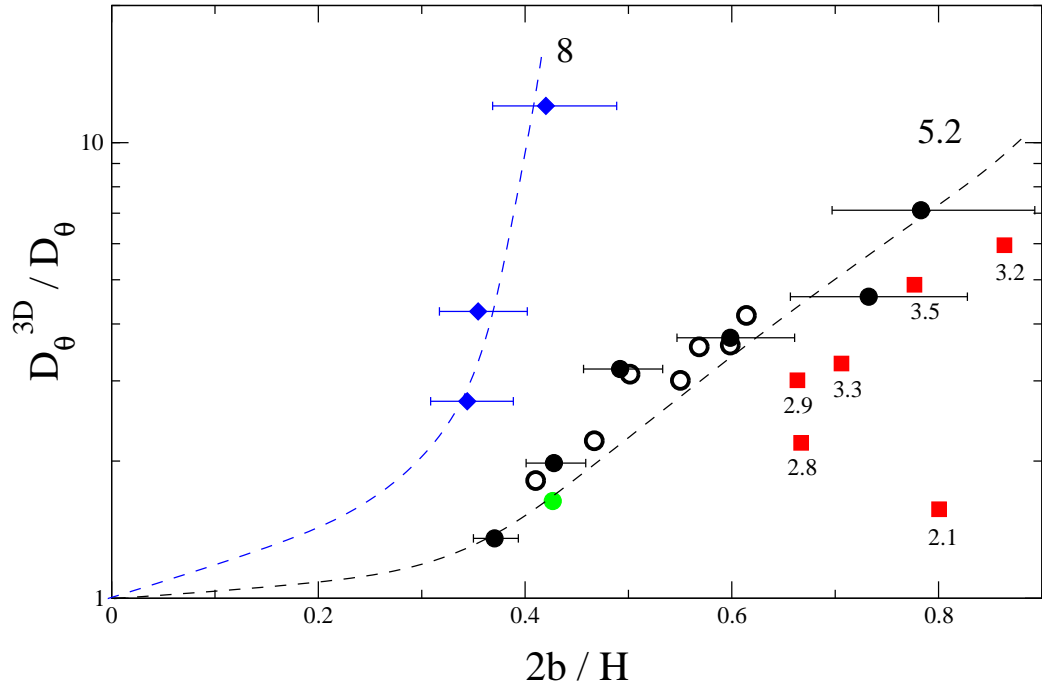


Figure S5: Ratio of theoretical rotational diffusion coefficient (5,6) D_{θ}^{3D} and measured diffusion coefficient D_{θ} under different confinement $2b/H$. Symbols are the same as those in Fig. S3.

References

1. C. C. Ho, A. Keller, J. A. Odell, R. H. Ottewill, *Colloid Polym. Sci.* **271**, 469 (1993).
2. J. C. Crocker, *Ph.D. Thesis* (the University of Chicago, 1996).
3. N. H. Hartshorne, A. Stuart, *Crystals and the Polarising Microscope*, 4th edition (Edward Arnold Ltd., London, 1970).
4. J. C. Crocker, D. G. Grier, *J. Colloid Interface Sci.* **179**, 298 (1996).
5. F. Perrin, *J. de Phys. et Rad.* **V**, 497 (1934).
6. S. Koenig, *Biopolymers* **14**, 2421 (1975).
7. J. Happel, H. Brenner, *Low Reynolds Number Hydrodynamics* (Kluwer, Dordrecht, 1991).
8. S. Bhattacharya, J. Blawdziewicz, E. Wajnryb, *J. Fluid Mech.* **541**, 263 (2005).